Journal of Theoretical Biology 300 (2012) 277–291

Contents lists available at SciVerse ScienceDirect

Journal of Theoretical Biology

journal homepage: www.elsevier.com/locate/yjtbi

Cargo distributions differentiate pathological axonal transport impairments

Cassie S. Mitchell*, Robert H. Lee

Wallace H. Coulter Department of Biomedical Engineering, Georgia Institute of Technology and Emory University School of Medicine, Atlanta, GA 30332, USA

ARTICLE INFO

Article history:
Received 19 September 2011
Received in revised form
22 December 2011
Accepted 11 January 2012
Available online 25 January 2012

Keywords:
Neurofilament
Molecular motor
G93A SOD1 model
Transgenic mouse
Motoneuron disease

ABSTRACT

Axonal transport is an essential process in neurons, analogous to shipping goods, by which energetic and cellular building supplies are carried downstream (anterogradely) and wastes are carried upstream (retrogradely) by molecular motors, which act as cargo porters. Impairments in axonal transport have been linked to devastating and often lethal neurodegenerative diseases, such as Amyotrophic Lateral Sclerosis, Huntington's, and Alzheimer's. Axonal transport impairment types include a decrease in available motors for cargo transport (motor depletion), the presence of defective or non-functional motors (motor dilution), and the presence of increased or larger cargos (protein aggregation). An impediment to potential treatment identification has been the inability to determine what type(s) of axonal transport impairment candidates that could be present in a given disease. In this study, we utilize a computational model and common axonal transport experimental metrics to reveal the axonal transport impairment general characteristics or "signatures" that result from three general defect types of motor depletion, motor dilution, and protein aggregation. Our results not only provide a means to discern these general impairments types, they also reveal key dynamic and emergent features of axonal transport, which potentially underlie multiple impairment types. The identified characteristics, as well as the analytical method, can be used to help elucidate the axonal transport impairments observed in experimental and clinical data. For example, using the model-predicted defect signatures, we identify the defect candidates, which are most likely to be responsible for the axonal transport impairments in the G93A SOD1 mouse model of ALS.

1. Introduction

Axonal transport has been implicated in motoneuron disease for over 40 years. Given the extremely long axons of motoneurons and their dependence on axonal transport for the delivery ATP-producing mitochondria and other essential constituents, it comes as no surprise that transport deficiencies cause debilitating effects. However, it was not until the 1990s, when defective axonal transport was shown to be present in the super-oxide dismutase-1 (SOD1) mouse model of Amyotrophic Lateral Sclerosis (ALS) that the potential clinical ramifications of axonal transport in pathology came to light. For the past twenty years, scientists and physicians have aggressively pursued identification of specific axonal transport defects and impairments in motoneuron diseases (MND) such as ALS, Charcot-Marie-Tooth (Brownlees et al., 2002; Baloh et al., 2007), Hereditary Spasticity Syndrome (Ferreirinha et al., 2004; Kasher et al., 2009), as well as neurological disorders, including Parkinson's (Saha et al., 2004; Ittner et al., 2008), Huntington's (Feany and La Spada, 2003; Morfini et al., 2009a,b), and Alzheimer's Diseases (Wang et al., 2010; Kim et al., 2011). Yet, the identities, origins, mechanisms, and implications of axonal transport in these diseases remain largely unresolved (Morfini et al., 2009a,b; Sau et al., 2011). For recent reviews, please see (De Vos, et al., 2008; Morfini et al., 2009a; Sau et al., 2011).

Based on current experimental evidence and hypotheses corresponding to said evidence, potential axonal transport impairments can be categorized into four basic types as shown in Fig. 1: binding defects (Xia et al., 2003; Teuchert et al., 2006), motor protein regulation (Jiang et al., 2005; Shi et al., 2010), energy deficits (Ellis et al., 2003; Fergani et al., 2011), and protein aggregation (Julien and Mushynski 1998; Hart, 2006). Possible types of axonal transport binding defects, potentially induced by mutations, could include inability of ATP to bind to the molecular motor (Brady, 1985), inability of the cargo to bind to the molecular motor (Misko et al., 2010), and inability of the molecular motor to bind to the microtubule (Morfini et al., 2002; LaPointe et al., 2009), all of which would result in non-processivity of the motor-cargo complex. Motor protein regulation controls the number of molecular motors present and available for transport at any one time. Changes in genetic expression, such as has been seen in KIF5 (Xia et al., 2003) in ALS or polyQ-htt (Lee et al., 2004) in Huntington's disease, can result in the increased or

* Corresponding author. Tel.: +1 404 276 8475.
E-mail address: cassie.mitchell@bme.gatech.edu (C.S. Mitchell).

0022-5193/$ - see front matter © 2012 Elsevier Ltd. All rights reserved.
doi:10.1016/j.jtbi.2012.01.019

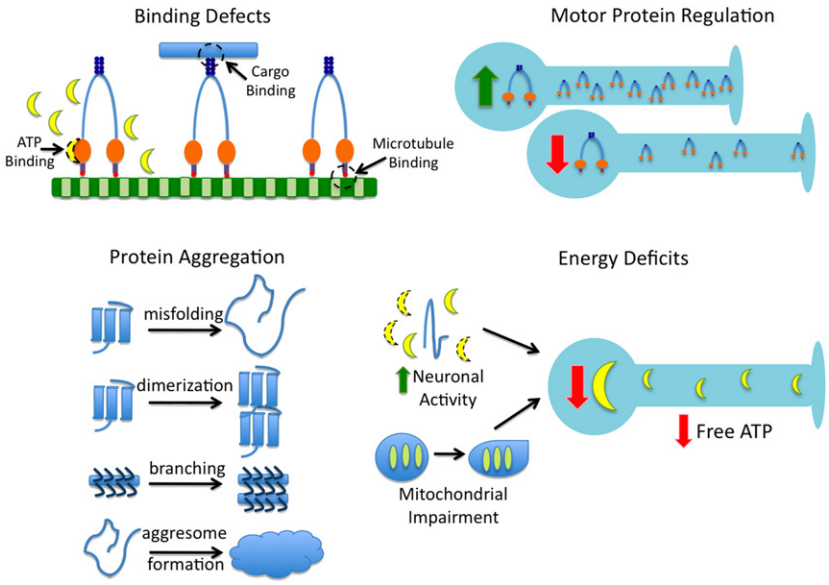

Fig. 1. Identified and hypothesized mechanisms of axonal transport impairment. *Binding defects* include an ability of ATP to bind to the motor, inability of the motor to bind to the cargo, and inability of the motor to bind to the microtubule. *Motor protein regulation* can be altered due to compensatory or aberrant genetic up- or down-regulation, resulting in an increase or decrease in the number of motors available for transport. Protein aggregation is concomitant with axonal transport impairment, and results from protein aggregates such as misfolded proteins (e.g. SOD1), aberrant dimers, neurofilament cross-linking, and by-products such as enlarged aggregsomes, which attempt to compensate by degrading excess aggregates. *Energy deficits* result in decreased free ATP available for motors, due to either increased ATP usage within the neuron or decreased ATP production due to mitochondrial impairment or aberrant regulation.

decreased availability of molecular motors, i.e. motor depletion (Gunawardena and Goldstein, 2001). Energy deficits can be caused by increased neuronal activity (Ackerley et al., 2000), such as is seen with excitotoxic pathways (Mitchell and Lee, 2008), or underproduction of ATP, corresponding to mitochondrial impairment or deficient mitochondrial regulation (Cai et al., 2011). Finally, protein aggregation is typically concomitant with all axonal transport impairments and includes protein misfolding, such as misfolded SOD1 (Morfini, 2009a) or tau (Sinadinos et al., 2009); aberrant dimerization (Elam et al., 2003); aberrant neurofilament branching and cross-linking (Miller et al., 2002; Ackerley et al., 2003); and increased aggresome formation (Strom et al., 2008).

A rather large roadblock in pathological research has been the inability to differentiate potential axonal transport impairment candidates from each other using collected experimental transport data. In this study, we utilize an analytical approach to differentiate three general impairment types based solely on the pathological transport data measures themselves. To provide controlled pathological transport datasets for analytical discrimination, we utilized our published experimentally-derived computational model (Mitchell and Lee, 2009) of physiological axonal transport and individually and conceptually overlaid three different impairment scenarios: (1) protein-aggregation; (2) motor population depletion (reduced kinesin and/or dynein); and (3) motor population dilution due the added presence of a non-functional, defective motor subpopulation. The goal of this work was to determine the general signature of each of these defects. We conclude that cargo distributions (e.g. positional distribution of cargos after an injected "pulse" or a given set of initial conditions, such as nerve ligation), cargo state analysis (i.e. quantity of cargos traveling net retrograde or net anterograde), and cross-correlation "landscapes" of axonal transport metrics successfully distinguish among these three impairment scenarios, even at impairment severities as low as 10%. Finally, we use the identified defect signatures to elucidate the potential defect candidates which could be responsible for the host of experimentally identified axonal transport impairments observed in the SOD1 mouse model of ALS.

2. Methods

We utilized our previously published physiological axonal transport model (Mitchell and Lee, 2009) as the underlying physiological foundation. However, for this study, we added multi-motor cooperativity (multiple motors working together to tow a single cargo) to allow the number of bound motors to the microtubule to dynamically change, ATP-dependence, and the effects of cargo load size. Using this physiological foundation, we then conceptually overlay three experimentally-based, hypothesized impairment types (protein aggregation, motor depletion, and motor dilution) to simulate pathological transport.

2.1. Impairment types

Theoretical models of pathological transport (Gazzola et al., 2009; Kuznetsov, 2010) are far less common than their physiological counterparts, likely due to scientific gaps in the field. In fact, the underlying pathological mechanisms of identified and hypothesized axonal transport defects in neurodegenerative diseases, including ALS, has yet to be revealed. Therefore, a first principles or mechanistic modeling approach to implement and examine specific axonal transport defects is not feasible at this time. Thus, while we utilized an experimentally-derived, mechanistic model of physiological axonal transport as the foundation (Mitchell and Lee, 2009), we chose to employ a conceptual or "top-down" (Shapiro and Lee, 2007) modeling approach to implement and individually examine three general types of axonal transport defects: protein aggregation, motor depletion, and motor dilution.

These defects are based on experimental evidence obtained from axonal transport studies in motoneuron diseases, namely the SOD1 transgenic mouse model of ALS. The identified impairments of protein aggregation, motor depletion, and motor dilution are hypothesized to exist alone and/or in combination in various pathologies such as ALS, Alzheimer's, and Huntington's. However, to date, the specific impacts of protein aggregation, motor depletion, and motor dilution have been experimentally indiscernible. The goal of this study was to capture the fingerprint or signature of

each of these defects. Thus, in the model, the defects are mathematically separated. By keeping the defects separated, predictions can be made as to when pathological systems switch or obtain an additional defect (e.g. only protein aggregation versus protein aggregation leading to motor depletion—see Section 4). The impairment concepts are described below and illustrated in Fig. 2.

2.1.1. Protein aggregated cargo population

As the name implies, an aggregated cargo population represents cargos, which are themselves protein aggregates or products of protein aggregation. As shown in Fig. 1, the main protein aggregates are misfolded proteins such as SOD1 (Hart, 2006), aberrant dimmers (Elam et al., 2003), or cross-linked or mutant neurofilaments such as is seen with mis-regulation of the NF-H, NF-M or NF-L chains that comprise neurofilaments (Julien and Mushynski, 1998). Enlarged aggresomes, due to compensatory degradation of misfolded or aberrant proteins, are a by-product of protein aggregation. Conceptually, each of these cargo types can be modeled as a simple increase in the normal load size (Fig. 2B). Whereas the normal (typically referred to as "wild-type" in experimental literature) cargo distribution, is approximately 0.1–4 pN, we represent protein aggregation as a cargo distribution of 0.1–10 pN, indicative of the formation of dimers.

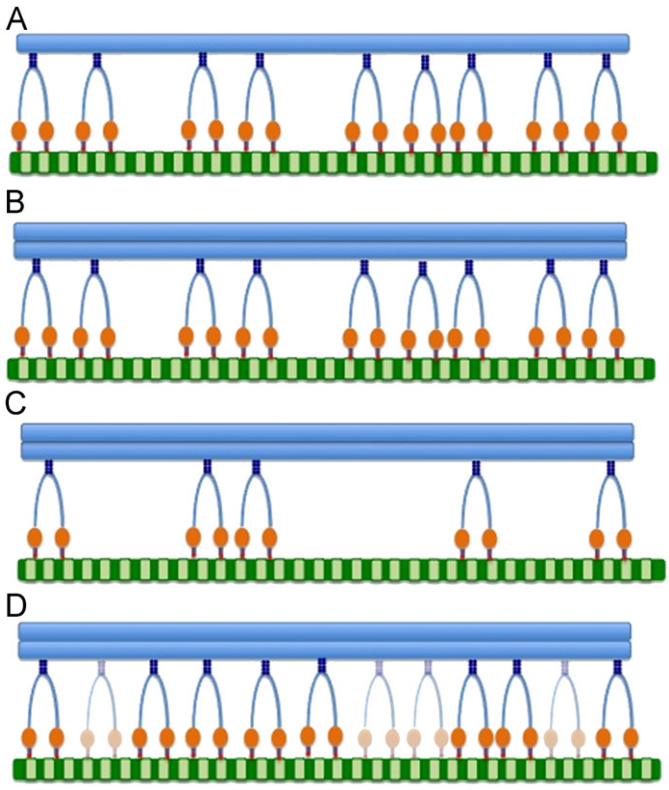

Fig. 2. Model concepts utilized to examine pathological axonal transport. (A) Physiological or "wild-type" axonal transport. All motors are fully functional, and there is an adequate motor population to maintain transport of normal or non-aggregated cargos. (B) Protein aggregation axonal transport. In this particular case, the cargo is a protein aggregate, represented by an increase in load size. The size of the motor population is the same as the wild-type case, and all motors are fully functional. (C) Depleted axonal transport. There is simply an inadequate number of motors to maintain normal transport. Shown with concomitant protein aggregation. (D) Diluted axonal transport. While an adequate or even a surplus population is available, a specified fraction of motors are non-functional, resulting in a "diluted" population. Shown with concomitant protein aggregation.

2.1.2. Depleted motor population

A depleted motor population is defined as an *inadequate* number of molecular motors to maintain normal transport. Thus, conceptually, a depleted motor population represents a motor population of which a specified fraction of motors are absent (Fig. 2C). This absence could be, for example, due to down regulation of motor proteins. Depletion could be specific to either kinesin or dynein or affect both motors. Here we examine each of these cases.

2.1.3. Diluted motor population

A diluted motor population is defined as a surplus number of motors that have been inter-mixed or "*diluted*" by the presence of a specified fraction of non-functional motors. Thus, conceptually, a diluted motor population represents up-regulated motor population, of which a percentage of motors have binding defects (Fig. 2D). Mutations could potentially affect either one or both motor types, depending on their specificity (Barkus et al., 2008). When applied to specifically to either kinesin *or* dynein, this implementation represents population-specific mutations. With motor dilution applied simultaneously to both kinesin and dynein, the implementation represents defective shared cargo adapters or defective ATP machinery. Cargo adapters are proteins that link the motor to the cargo, providing specificity and directionality. Example cargo adapters include Milton, which transports mitochondria (Magrane and Manfredi, 2009) and dynactin (LaMonte et al., 2002). We examine dilution of each motor population individually as well as collectively.

2.2. Physiological axonal transport model

Using pulse-labeling experiments and/or nerve ligation, physiological axonal transport has been extensively examined, and several theoretical models have been built that successfully recapitulate experimental findings (Brown et al., 2005; Craciun et al., 2005; Klumpp and Lipowsky, 2005; Muller et al., 2008; Mitchell and Lee, 2009). The field recognizes four main types of transport (Brown et al., 2005), which are largely categorized based upon the average cargo velocities, but also loosely based upon cargo type and direction: fast anterograde or retrograde, fast bi-directional, and slow components (A and B), shown in Table 1. A fifth transport type, intermediate transport, while less frequently mentioned, is known

Table 1
Axonal transport types, velocities, and cargos.

Transport type	Velocity (mm/day)	Velocity (μm/s)	Example cargo type (s)
Fast			
Anterograde	200–400	2.31–4.63	Golgi-derived vesicles, tubules, neurotransmitters
Retrograde	200–400	2.31–4.63	Enodosomes, lysosomes
Bidirectional	50–100	0.58–1.16	Mitochondria
Intermediate	8–50	0.08–0.58	Intra-axonal proteins
Slow			
Component A	0.3–3	0.003–0.035	Neurofilaments
Component B	2–8	0.02–0.08	Microfilaments, actin

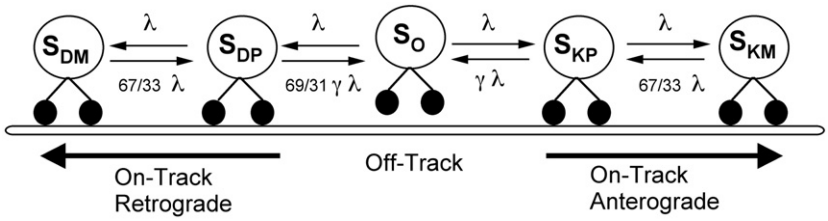

Fig. 3. Schematic of physiological axonal transport model (Mitchell and Lee, 2009). The model contains five states, *S*, which are differentiated using the following subscript nomenclature: *P* represents a paused motor, *M* represents a moving motor, *K* represents the molecular motor kinesin, *D* represents the molecular motor dynein, and *O* represents an off-track motor. Using this nomenclature, we obtain the following states: (S_O) off-track, paused; (S_{KP}) kinesin, on-track, paused; (S_{DP}) dynein, on-track, paused; (S_{KM}) kinesin, on-track, moving anterogradely; (S_{DM}) dynein, on-track, moving retrogradely. The rate constants λ and γ, were tuned to obtain a velocity distribution ranging from slow through fast bi-directional transport.

to exist and is comprised of intra-axonal proteins traveling at speeds between those of slow and fast transport.

In the physiological model, we utilize experimental pulse-labeling kinetics to examine transport of cargos from slow transport (e.g. neurofilaments) through fast bi-directional transport (e.g. transport of mitochondria). We incorporate the pulling effect of multiple motors working together, as well as ATP-dependent stall forces. Each of these features is discussed in detail in the following sections. The order of operations is as follows: first, the experimentally-based kinetics are used to determine the cargo state (Fig. 3) and state duration time. Next, the number of bound motors working together to a pull a cargo (e.g. cooperativity) is calculated. Subsequently, the ATP concentration and cargo size are used to calculate the individual motors' stall force. Finally, the number of bound motors, the kinetic binding rates, and the stall force are used to calculate the cargo's velocity. This process is repeated for all cargos until the simulated time of 1000–3600 s is reached.

2.2.1. Kinetics

Experimental studies of physiological transport have shown that the differences in velocity among transport types are largely due to the number of pauses and pause duration (referred to as the stop-and-go hypothesis (Brown et al., 2005)), with the rate of directionality change playing a smaller role. Thus, mechanistic physiological models of axonal transport, such as the model (Mitchell and Lee, 2009) utilized in this study, are typically comprised of on-track anterograde or retrograde, paused anterograde or retrograde, and off-track states. Just like their experimental counterparts, the kinetic rates of switching among these states determine whether the computational model emulates fast or slow transport. We utilize the aforementioned kinetic states as the platform for examining physiological axonal transport and as the underlying foundation for examining pathological transport.

Our previously published model (Mitchell and Lee, 2009) adapts experimental transport kinetics described by (Craciun et al., 2005) in order to obtain physiological average velocities that take into account different possible motor-microtubule kinetic states. This scheme describes both retrograde and anterograde transport using the following five states as shown in Fig. 3: S_O—off-track, paused; S_{KP}—kinesin, on-track, paused; S_{DP}—dynein, on-track, paused; S_{KM}—kinesin, on-track, moving anterogradely; S_{DM}—dynein, on-track, moving retrogradely. The scheme is such that a cargo must disengage from the track before switching directions, and it must pass through an on-track paused state before moving.

The kinetic scheme was implemented using event-based simulation (Banks et al., 2005), a method that speeds simulation time by avoiding unnecessary repetitive calculations by predicting how long a cargo will remain in the same state. The expected duration of each possible state, t_{state}, is calculated by multiplying the inverse of the state's rate constant, k, by the natural log of a random number, *rand*, in the range 0–1 exclusive giving

$$t_{state} = -1/k \ln(rand) \quad (1)$$

The form of Eq. (1) is chosen to fit the exponential first order process that is apparent in experimental data (Wang and Brown, 2001) as published in Table 1 of (Brown et al., 2005). The state with the shortest duration becomes the next state for that cargo. Based on the duration of the cargo's current state and the current time in the simulation, a sorted list determines when each cargo should be re-evaluated so that not every cargo need be evaluated at every time step.

Rate constants were adjusted from those originally published by (Craciun et al., 2005) (i.e. λ and γ and were varied while all other parameters were held constant) to fit our model implementation and to experimentally match velocity profiles for slow through bi-directional transport.

2.2.2. ATP dependence

ATP dependence was modeled using a constant ATP concentration. The ATP-dependent stall force, F_s, of kinesin and dynein was adapted from Gao (2006). For all simulations, except the landscape analysis, constant physiological ATP concentration of 1000 μM was used giving dynein an approximate 1 pN stall force and kinesin an approximate 5 pN stall force, comparable to experimental findings (Kural et al., 2005; Gao, 2006). In order to determine how ATP correlates with other key model outputs, ATP was varied $\pm 50\%$ in the sensitivity analysis utilized to make the cross-correlation landscapes.

2.2.3. Multi-motor cooperativity

"Cooperative transport" is defined as transport in which motors of the same type work together to pull a load. In this study, 1–12 motors of the same type can work together to pull cargo. There have been different concepts used to model or implement cooperative transport, such as coordinated switching between the kinesin and dyenin populations, tug-of-war between bound kinesins and dyneins, where the motor population exerting the most force "wins", and kinetic-based schemes using pulse-labeling experimental data. Here we implement a kinetic-based scheme using the experimentally determined probabilities of Brown and Wang to calculate the probability that the cargo will travel anterograde or retrograde, and we use the determined cargo direction or state to determine which motor population type (kinesin or dyenin) is bound. Note that these probabilities correspond to the directionality rate parameter, as described in Mitchell and Lee (2009) and Craciun (2005).

The number of motors of each type bound to the microtubule for each cargo is determined by the equation proposed by Klumpp and Lipowsky (2005) (Eq. (8)), which assumes dilute enough motor coverage that exclusion effects are negligible. The number of bound motors, N_b, is a function of the motor to microtubule

binding (π_{AD}) and unbinding (ε) rates, the previous state's number of bound motors (n), the maximum allowable number of motors able to bind (N), the load (F), the detachment force, F_d=3 pN (Klumpp and Lipowsky, 2005), and the stall force (F_s). The binding and unbinding rates are determined by the kinetic rates used to calculate the state duration. The maximum allowable number of bound motors is 12 per cargo, as determined by experimental evidence from Kural et al. (2005). We utilize experimentally-determined kinetics, specifically the directionality rates X and Y, to determine whether the calculated number of bound motors are dynein or kinesin.

$$N_b = \frac{(\pi_{ad}/\varepsilon)[1+(\pi_{ad}/\varepsilon)]^{N-1}}{[1+(\pi_{ad}/\varepsilon)]^{N}-1} \tag{2}$$

2.2.4. Cargos

Neurofilaments, intra-axonal proteins, and bi-directional transport of mitochondria are three key cargo types that are affected by axonal transport defects, according to experiments investigating axonal transport in the SOD1 mouse model of ALS (Sasaki et al., 2004). Since not all transport ranges can be examined in the same transport model due to their vastly differing transport kinetics, we focus this study on three aforementioned key cargo types, which have a transport range of slow through fast bi-directional transport (refer to Table 1). Thus, the model presented here does not directly examine the fasted end of the axonal transport spectrum. Given these affected cargo types, we utilize a large population (1000–10,000) of various cargos sizes to represent different cargo types, and we correspondingly select kinetic rate constants that result in a cargo distribution undergoing slow through fast bi-directional axonal transport (see kinetics).

Each cargo's size (F) was randomly determined over a set range starting at a minimum of 0.1 pN (Gao, 2006); using the experimental data from Wang and Brown (2001) as given in Brown et al. (2005) as the target output to tune the model, the maximum cargo size for "normal" transport was set to 4 pN. To model the effect of an increased load due to protein aggregation and/or misfolding, we expand the range to 10 pN. This approximation was based on the formation of dimers (Elam et al., 2003). The effect of load on the unbinding rate is calculated as described by Klumpp and Lipowsky (2005)

$$\varepsilon(F) = n\varepsilon \exp\left(\frac{F}{nF_d}\right) \tag{3}$$

2.2.5. Velocity

Based on the approximate linear proportional relationship of the number of bound motors to velocity as illustrated in the experimental data (Kural et al., 2005), we obtain the velocity for a cargo, i, as a function of the number of motors bound, load, and the ATP-dependent stall force. v_{const} is the average uncorrected constant velocity of kinesin and dynein, 1 μm/s (Klumpp and Lipowsky, 2005)

$$V_i = v_{const}\left[1-\frac{F_i}{N_{b,i}F_{s,i}}\right]N_{b,i} \tag{4}$$

2.3. Pathological axonal transport model

A conceptual modeling approach was utilized to overlay different axonal transport impairment scenarios on the physiological axonal transport foundation. Protein aggregation was modeled utilizing an increased load size (see cargos). A depleted motor population was modeled by decreasing the total motor population available to bind to cargos, and a diluted motor population was created by increasing the total motor population available to bind to cargos and by specifying a portion of that population to be defective, or non-functional. The depleted and diluted motor populations were applied either individually to kinesin or dynein for simulations examining the effect of depleting a single population and simultaneously for simulations examining depletion of both motor types. The depleted and diluted methods are described in detail below.

2.3.1. Specifying the motor population

In the real axons, the total number of molecular motors and the percentage of which are ineffective depends on the type and degree of dysfunction resulting from protein deregulation or mutations. We model the availability of motors for the "depleted" and "diluted" cases using conservation balances where the total number of motors and the percentage of motors deemed "functional" are specified. A constant factor, k_T, is used to scale the total number of motors in the population, M_{total}, with "just enough" motors defined as k_T=1 as described by Eq. (1). The total number of cargos, C_{total}, is 10,000. The maximum allowable number of motors per cargo, N, is 12. (see Section 2.2.3).

$$M_{total} = C_{total}Nk_T \tag{5}$$

Similarly, a functional motor factor, k_F, is used to specify the percentage of total motors deemed "functional" (Eq. (2)) with 100% functionality described as k_F=1

$$M_{F,total} = M_{total}k_F \tag{6}$$

Conservation balances (Eqs. (3)–(5)) are used to keep track of how many functional ($M_{F,avail}$), non-functional ($M_{NF,avail}$), and total motors ($M_{total,avail}$) are available to be assigned to a cargo

$$M_{F,avial} = M_{F,total} - \sum_{i=1}^{i=C_{total}} M_{F,i} \tag{7}$$

$$M_{NF,avial} = M_{NF,total} - \sum_{i=1}^{i=C_{total}} M_{NF,i} \tag{8}$$

$$M_{total,avial} = M_{F,avial} + M_{NF,avial} \tag{9}$$

Given availability, the maximum total number of motors that can be assigned to any one cargo is specified by N (see Section 2.2.3), and the number of functional and non-functional motors for each cargo is assigned randomly using k_F as the probability criterion (i.e. if a random number between 0 and 1 is less than or equal to k_F, the motor assigned is functional).

2.3.2. Example of how impairment severities determine depleted and diluted populations

Depleted populations have an overall lower total number of motors compared to wild type. For example, a 90% severity would have 90% fewer motors available compared to wild type. However, all of the motors would be functional. A diluted case has more motors available than wild type, but a portion of them are non-functional. For example, diluted population of 90% severity has a total motor population that is ten times larger (k_T=10) than the wild type case, but 90% of this population is comprised of ineffective motors (e.g. dilution severity of 90%). Thus, the total number of functioning motors in the diluted case is actually equivalent to the wild type case.

2.4. Analysis and implementation

Cargo distributions illustrate the number of cargos per position bin versus position (μm). They are based on the final position of each

Table 2
Identification, type, description of outcome measures and parameters in the depleted and diluted landscapes of Fig. 10. O=output, P=parameter, P/O=parameter and an output (e.g. parameter is initially set but then changes based on dynamics within the model).

Measure ID	Type	Description
KD ratio	P/O	Ratio of anterograde to retrograde sub-populations
AvgVel	O	Average cargo velocity (μm/s) over the simulation duration
KAvgVel	O	Average velocity of anterogradely moving cargos
KAvgNb	O	Average number of bound kinesin
MaxPos	O	Largest final position magnitude obtained by an anterogradely moving cargo
Brown1750	O	Number of cargos moving at 1750 nm/s (Brown et al., 2005)
Brown2750	O	Number of cargos moving at 2750 nm/s (Brown et al., 2005)
Brown2250	O	Number of cargos moving at 2250 nm/s (Brown et al., 2005)
Brown1250	O	Number of cargos moving at 1250 nm/s (Brown et al., 2005)
Brown750	O	Number of cargos moving at 750 nm/s (Brown et al., 2005)
Brown250	O	Number of cargos moving at 250 nm/s (Brown et al., 2005)
N	P	Total number of motors assigned to each cargo (Klumpp and Lipowsky, 2005)
DAvgNb	O	Average number of bound dynein
#pause	O	Total number of pauses for the simulation duration
D#pause	O	Number of pauses during retrograde movement
MinLoad	P	Minimum cargo size utilized to calculate the distribution of cargo sizes
K#pause	O	Number of pauses during anterograde movement
DAvgVel	O	Average velocity of a retrogradely moving cargo
MinPos	O	Largest final position magnitude obtained for the simulation duration by a retrogradely moving cargo
AvgPause	O	Average pause duration
Severity	P	Severity of impairment (% decrease in motor population for depleted case and % of defective cargos for diluted case)
MaxLoad	P	Maximum cargo size in the cargo distribution
AvgLoad	P	Average load size of the cargo distribution
Brown0	O	Number of cargos not moving (Brown et al., 2005)
ATP	P/O	Average concentration of available ATP

cargo at the end of the specified simulation length (1000–3600 s). Simulations best mimic the analyses that are done in a nerve ligation study, where cargos are quantified on each side of the ligation. Cargo state analysis calculates the anterograde, retrograde, and stop sub-populations at the end of the specified simulation length. The output metric cross-correlations in the landscapes are based upon a sensitivity analysis of the parameter space.

Sensitivity analyses examine the behavior, or sensitivity, of a model over what is thought to be a realistic parameter range (Mitchell et al., 2007). For this study, all parameters were varied $\pm 50\%$ in the sensitivity analysis to create the outcome deviation slopes (e.g. how much each outcome metric changed compared to the wild type case) utilized to make the cross-correlation landscapes. For more details on the landscape methods, please see our previous publications (Mitchell and Lee, 2007, 2008). Parameters that were examined include the kinetic rate for motor directionality, kinetic rates for determining motor states (paused, moving, off-track), cargo size, individual motor velocity for kinesin and dynein, number of available motors, ratio of available kinesin to dynein motors, simulation duration, number of available cargos, and ATP concentration. Measured outputs are defined in Table 2.

The physiological and pathological models were implemented in Matlab (Mathworks, Inc.). Analysis was completed in IGOR (Wavemetrics, Inc.). Simulations were run on a Macbook Pro (Apple, Inc.) personal computer, 4 GB RAM.

3. Results

We have previously shown that cargo distributions (number of cargos versus their final position after an injected "pulse" or a specific set of initial conditions) can be utilized to examine important cargo population features of physiological axonal transport (Mitchell and Lee, 2009). Furthermore, distributions have been used to reliably reproduce or mechanistically investigate physiological axonal transport experimental findings (Brown et al., 2005). Here we utilize cargo distributions to compare physiological or "wild-type" axonal transport to pathological axonal transport. We utilized cargo distributions, in combination with cargo state analysis (number of cargos in the retrograde, stop, or anterograde sub-populations), and cross-correlation analysis of experimentally-derived transport metrics, to obtain a comprehensive view of pathological transport and its resulting dynamics. Moreover, we use the aforementioned analytical techniques to determine key identifying characteristics of each of the general impairment types of protein aggregation, motor depletion, and motor dilution.

3.1. Effect of protein aggregation on axonal transport

3.1.1. Protein aggregation slows cargo separation

Protein aggregation is modeled as an increase in the maximum load size from 0.1–4 pN to 0.1–10 pN and with the same quantity of motors and cargos as the wild-type case (see Section 2). At the simulated time of 1000 s, protein aggregation results in a single, unimodal distribution centered at 0 μm (Fig. 4B) compared to the bimodal distribution obtained with the wild-type case (Fig. 4A). Thus, the splitting of the total protein aggregated cargo population into retrograde and anterograde sub-populations has a definite delay in onset. Consequently, even at longer time frames when the protein aggregated case has had enough time to completely separate into anterograde and retrograde sub-populations, the wild-type case will still have a much larger gap between the two sub-populations (not shown). The overall scaled height of the aggregated cargo distribution remains similar to the wild-type case except for the bins close to 0 μm. The position range of the distribution (i.e. the minimum and maximum position as shown on the *x*-axes of Fig. 4) for the protein aggregation case remains relatively unchanged compared to the wild-type case. However, a closer examination of cargos on a per-size basis, reveals that positions of cargos of the same size are considerably more staggered compared to the wild-type case. For example, all cargos in the "0 pN" bin (Fig. 4B, purple, corresponding to cargo sizes <1 pN), have positions between ± 250 and 800 μm in the wild-type case, whereas in the protein aggregation case, the position range is ± 50–800 μm.

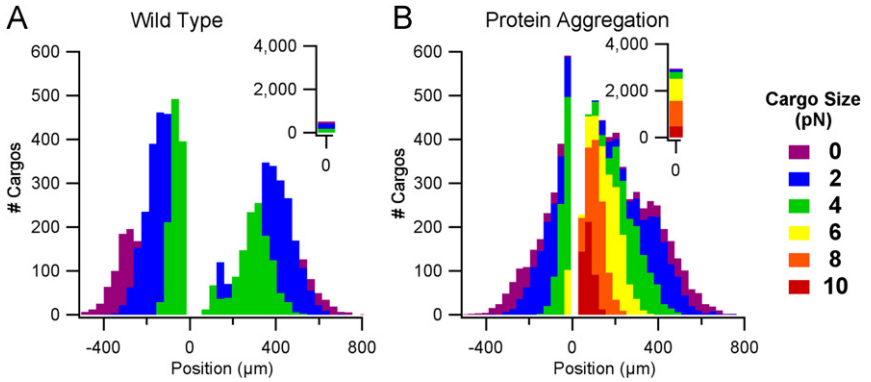

Fig. 4. Cargo distributions of wild-type compared to protein aggregation axonal transport. Both distributions contain 10,000 cargos and show the final cargo positions (μm) after 1000 s. Colors indicate cargo sizes (0.1–10 pN). A. Wild-type axonal transport with physiological cargo sizes ranging from 0.1–4 pN. B. Protein aggregation axonal transport with pathological cargo sizes ranging from 0.1–10 pN. (For interpretation of the references to color in this figure legend, the reader is referred to the web version of this article.)

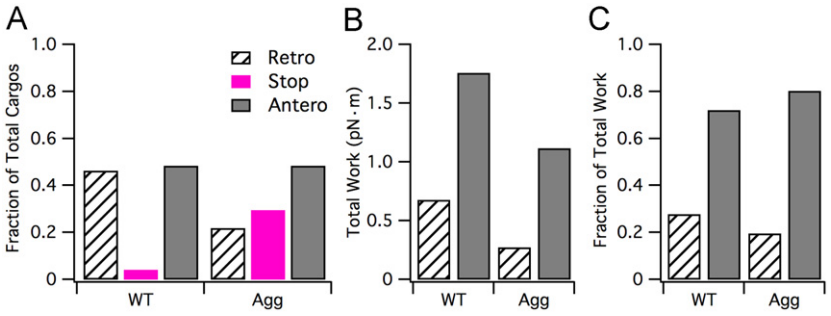

Fig. 5. Analysis of wild-type and protein aggregation cargo sub-populations. (A) Fraction of total cargos in each sub-population state (retrograde, stop, anterograde). (B) Total work (pN) performed by the anterograde and retrograde sub-populations, respectively, for wild-type and protein aggregation cases. (C) Fraction of total work utilized by anterograde and retrograde sub-populations for wild-type and protein aggregation cases.

3.1.2. Protein aggregation decreases retrograde cargo transport and increases cargo pausing

Breaking the cargo distributions into retrograde, stop (e.g. either cargos that are paused/off-track for the duration of the simulation or cargos whose final position is less than the experimentally expected minimum position for slow component A transport), and anterograde sub-populations is helpful for distinguishing how protein aggregation affects the cargo population state. As shown in Fig. 5A, the wild-type case fraction of cargos in the retrograde, stop, and anterograde states is 0.46, 0.04, and 0.5, respectively, whereas for protein aggregation the fractions are 0.3, 0.22, and 0.48, respectively. That is, the total fraction of cargos in the anterograde sub-population (e.g. all cargos whose final position is greater than 0 μm), is nearly equivalent between wild-type and protein aggregation cases. In contrast, there is over a 7-fold increase in the total fraction of cargos in the paused state (e.g. all cargos whose final position is in the "0 μm" bin) for the protein aggregation case compared to the wild-type case. Likewise, the total fraction of cargos in the retrograde state in the protein aggregation case is approximately half that of the wild-type case. Correspondingly, the simulation records reveal an increased number of total pauses for both motor types, but especially dynein. It is this increased number of pauses that results in the decrease of the retrograde sub-population and the increase in the stop sub-population exhibited with protein aggregation.

Additionally, we examined how protein aggregation affected the total work performed by the anterograde and retrograde sub-populations. The work (pN m) performed for each cargo was calculated by multiplying the cargo size (pN) by the distance traveled (converted from μm to m). The work performed for each cargo within its sub-population was summed to obtain the total work for the anterograde and retrograde sub-populations, respectively. The combined total work for both sub-populations is reduced by 50% in the case of protein aggregation compared to wild-type (e.g. combined total work of 1.4 pN m versus 2.4 pN m for WT, respectively). This equates to a 60% reduction in total retrograde work and a 30% reduction in total anterograde work in protein aggregation versus wild-type (Fig. 5B). The fraction of anterograde to retrograde work is approximately 2.5:1 for wild-type compared to 4:1 for protein aggregation (Fig. 5C).

3.2. Effect of depleted versus diluted motor populations on axonal transport

Given that protein aggregation is known to be concomitant with other axonal transport impairments, we chose to model the depleted and diluted cases using a cargo distribution indicative of protein aggregation, again with a load size 0.1–10 pN. Each case was modeled with 1000 cargos over a simulated time frame of one hour (3600 s). The protein aggregation case without subsequent depleting or diluting effects (referred to as the base case or 0% severity) is shown for reference in Figs. 6A and 7A.

3.2.1. Cargo distributions differentiate between impairment types

Motor protein deregulation, resulting in a decreased number of motors available for transport, is modeled as a depleted motor population. That is, the total population of motors is decreased by specified percentage, referred to as the severity.

A simultaneously depleted motor population of kinesin *and* dyenin results in changing the corresponding height of the

distribution over the simulated time frame. Thus, the heights of the non-zero bins decrease (i.e. fewer cargos per non-zero position bin) while the number of cargos in the zero bin increase. However, the position range of the affected cargo's distribution does not vary substantially from the base case. Thus, a decreased number of motors results in a substantial increase in the number of total cargos that are not moving compared to the normal case, but the positions of cargos that are moving remains similar to the base case. The depleted motor effect was quantitatively detectable with a mere 10% decrease in the motor population (e.g. severity=10%), and the effect was qualitatively or visually noticeable with a 30% decrease in the motor population (e.g. severity=30%). Fig. 6B–F illustrates how the depleted motor affect increases with severity for depleted severities of 10%, 30%, 50%, 70%, and 90%. Notice that even at 90% severity (Fig. 6F), the full spectrum of positions is unchanged, although the total number of moving cargos is quite small, as reflected by the dramatic decrease in the bin heights.

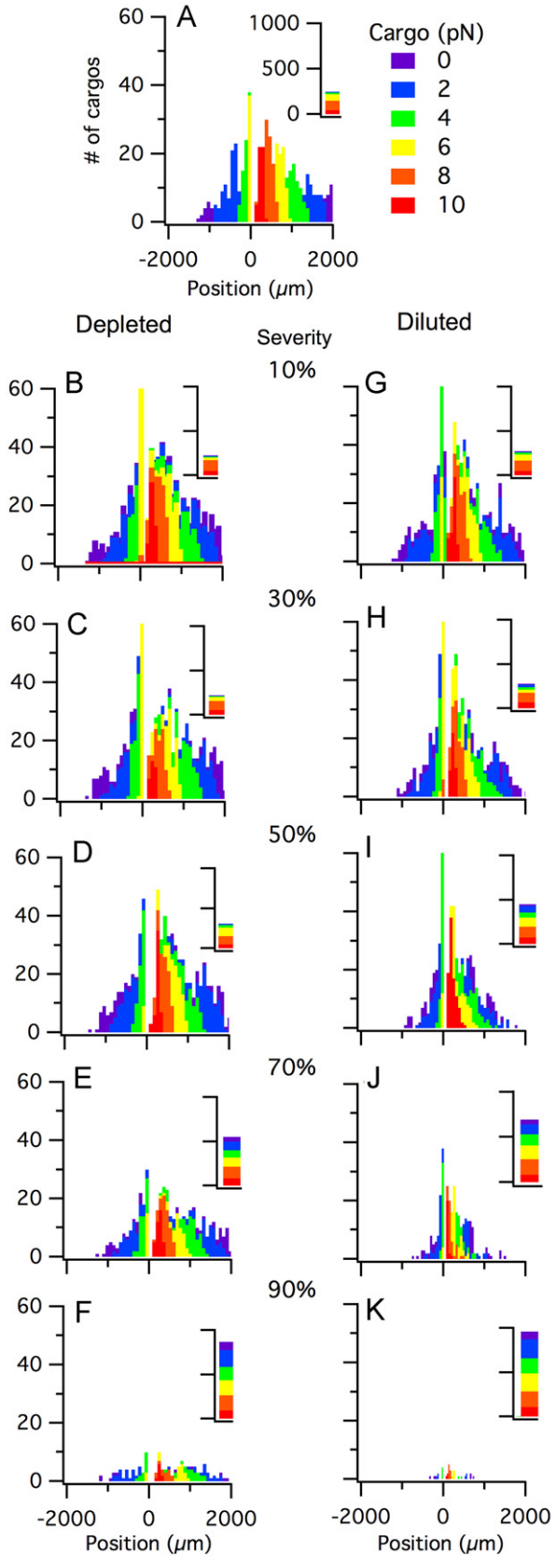

Looking at depletion in a single motor population, kinesin (Fig. 7B–D) *or* dynein (Fig. 7H–J), the same general trends follow but apply. There is increased pausing in the depleted population, but the overall velocities of the cargos that are moving remain unchanged. Thus, the position range of the affected population remains similar to base case. For the depleted kinesin population, only at the most severe severity (90%) is there a switch that favors additional retrograde transport (more cargos travel retrogradely in comparison to the base case). For the depleted dynein population, there is a favoring of anterograde transport at all impairment severities. This 10–15% shift towards additional anterograde transport remains approximately constant with depletion severity, with the exception of the most severe dynein depletion (90%).

Binding defects are indirectly modeled by diluting the motor population. The total number of available motors is greater than wild type (e.g. upregulated), but a portion of the total population is non-functional (unable to tow a cargo). For example, the diluted population shown in Fig. 6K has a total motor population that is ten times larger ($k_T=10$) than the normal case, but 90% of this population is comprised of ineffective motors (e.g. dilution severity of 90%). Thus, the total number of functioning motors in this example is actually equivalent to the wild type case.

Simultaneously diluting both the number of kinesin *and* dynein, by introducing motors into the population that contain binding defects rendering them non-functional, results in decreasing the heights of the non-zero bins and in decreasing the position range of the distribution (Fig. 6G–L). That is, at all levels of dilution severity, there are fewer total cargos that are moving compared to both the base and depleted cases; additionally, those cargos that are moving are doing so at a slower overall velocity, resulting in an often substantial decrease in the cargo distribution position range. Thus, having an ample number of motors, of which a portion are ineffective, results in a much more severe axonal transport impairment compared to simply depleting the motors. Even when looking at a diluted population over as little time as 1000 s (approximately 1/3 of the simulation time shown in Fig. 6G–L), the effects of dilution becomes quite noticeable when the ratio of total motors to functional motors is as low as 3:1 and increases proportionally as the number of total motors is increased and the number of functional motors is held constant.

Examining individual depletion of either kinesin (Fig. 7B–D) *or* dynein (Fig. 7H–J), the same general dilution trends are seen. Solely

Fig. 6. Cargo distributions for depleted and diluted impairments that affect both kinesin and dynein (with concomitant protein aggregation). All distributions contain 1000 cargos and show the final cargo positions (μm) after one hour. Colors indicate cargo sizes (0.1–10 pN). (A) No defects (e.g. 0% severity). Shown for comparison. (B–F) Depleted motor populations at 10%, 30%, 50%, 70%, and 90% severity, respectively. Severity (%) indicates the specified amount by which the motor population was depleted (e.g. percentage decrease in motor population). (G–K) Diluted motor populations at 10%, 30%, 50%, 70%, and 90% severity, respectively. Severity (%) indicates the specified amount by which the motor population was diluted (e.g. percentage of defective or non-functioning motors). (For interpretation of the references to color in this figure legend, the reader is referred to the web version of this article.)

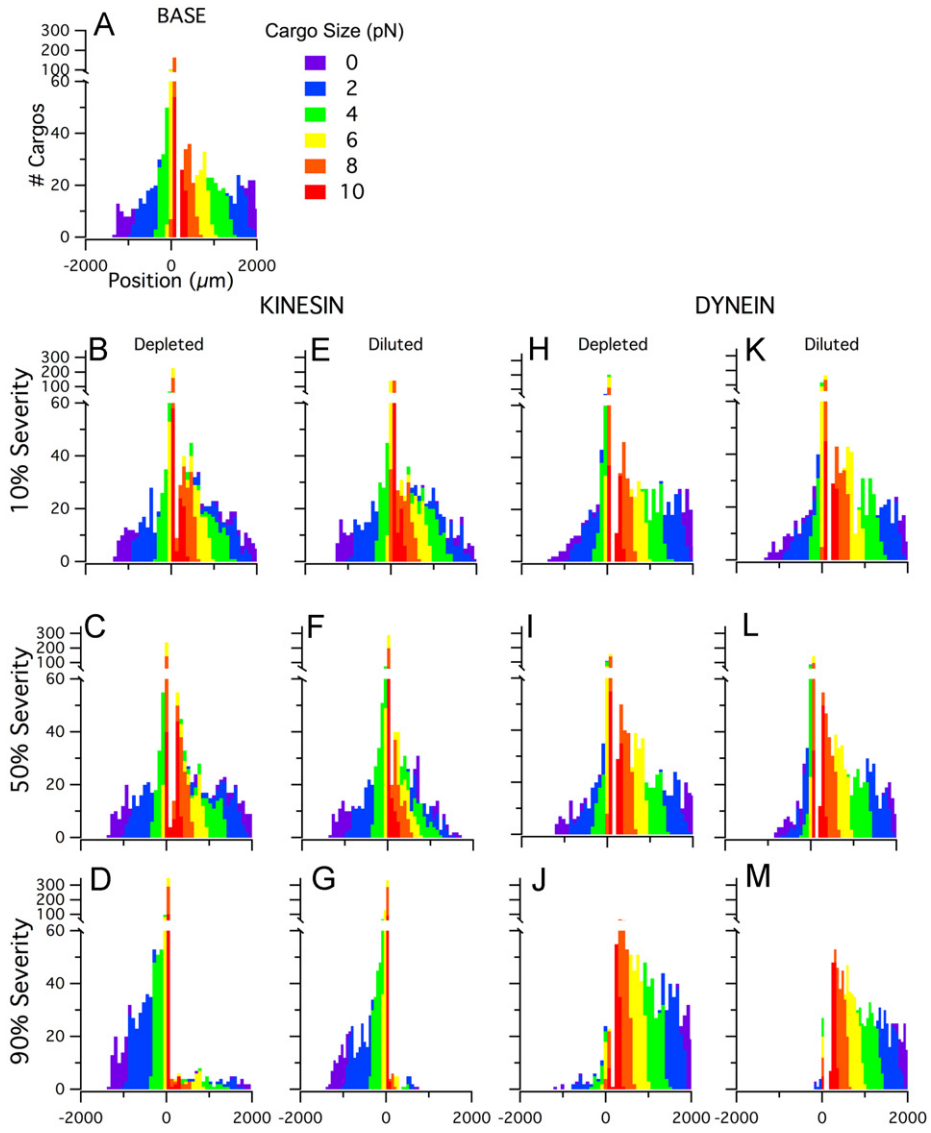

Fig. 7. Cargo distributions for depletion and dilution impairments that affect either kinesin or dynein (with concomitant protein aggregation). All distributions contain 1000 cargos and show the final cargo positions (μm) after one hour. Colors indicate cargo sizes (0.1–10 pN). (A) No defects (e.g. 0% severity). Shown for comparison. (B–D) Depleted kinesin population at 10%, 50%, and 90% severity. (E–G) Diluted kinesin population at 10%, 50%, and 90% severity. (H–J) Depleted dynein at 10, 50, 90% severity. (K–M) Diluted dynein at 10%, 50%, and 90% severity. (For interpretation of the references to color in this figure legend, the reader is referred to the web version of this article.)

diluting kinesin *or* dynein, results in increasing the number of pauses in the diluted motor type and a reduction in overall velocity (or final position) of the corresponding affected cargos. That is, a diluted kinesin population results in a reduction of anterograde cargo position whereas a diluted dynein population results in a reduction of retrograde cargo position. Shifting of the transported cargo direction occurs with either kinesin (Fig. 7D) or dynein dilution (Fig. 7J), especially at higher impairment severities.

3.2.2. Cargo state analysis reveals impairment-specific transport fluctuations

Typically, in pathological studies of axonal transport, experimentalists keep track of the quantity of cargos moving in either the retrograde or anterograde direction, as well as the quantity of cargos whose final positions remain unchanged (e.g. paused or off-track). Therefore, cargo state analysis is important for comparing and contrasting depleted and diluted modeling results to the results of pathological experimental studies. We perform cargo state analysis on the base, depleted, and diluted cargo distributions shown in Figs. 6 and 7. Two separate, but similar analyses were performed. First, we calculated the fraction of the total population present in the retrograde, stop, and anterograde sub-populations for each severity. To further extract how depleting or diluting the motor population affects the sub-population content, we determined the factor difference of each sub-population from the base case (0% defective, but with concomitant protein aggregation) at each severity.

The cargo state analysis for simultaneous depletion of the kinesin *and* dynein motor population(s) is shown in Fig. 8A and C. For the 10% and 30% severity depleted cases, the retrograde sub-populations grew while the stop sub-populations proportionally shrunk; the anterograde population remained the same for the 10% severity case, while it slightly decreased for the 30% case. At 50% severity for the depleted case, a substantial sub-population flip occurred: the stop sub-population substantially increased while the retrograde sub-population proportionally decreased; correspondingly, the anterograde sub-population only shows a slight decrease. For the 70% and 90% severity cases, the depleted motor populations showed a dramatic increase in the stop sub-population and a proportional decrease of the retrograde and anterograde sub-populations. The ratio of the anterograde to

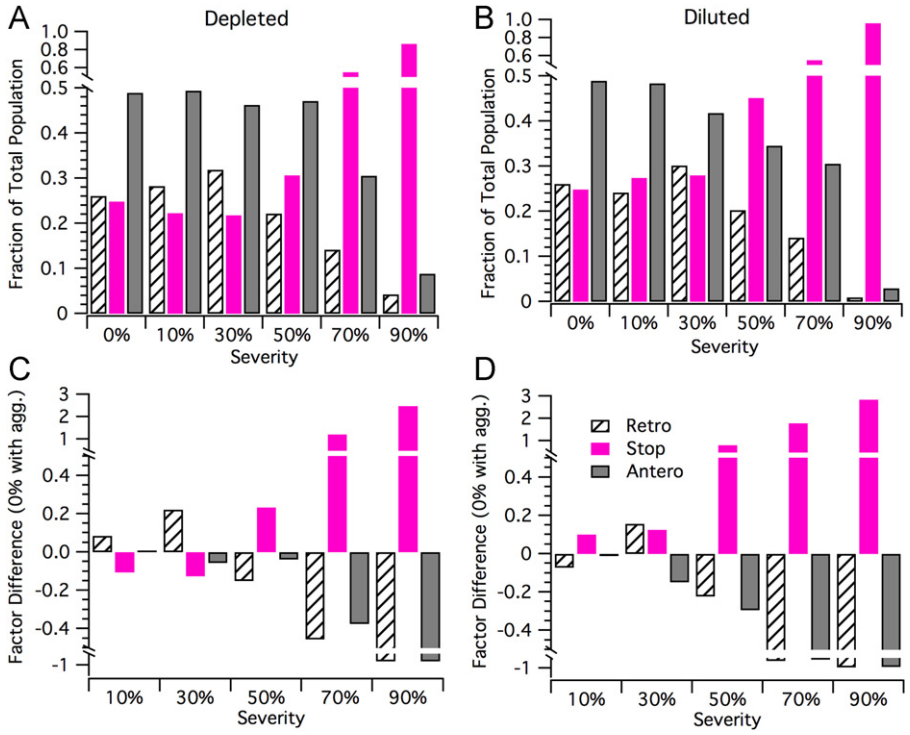

Fig. 8. Cargo state analysis for depletion or dilution impairments that affect *both* kinesin and dynein (with concomitant protein aggregation). (A and B) Fraction of total cargos in the retrograde, stop, and anterograde sub-populations for a depleted motor population at 0% (base), 10%, 30%, 50%, 70%, and 90% severities for depleted and diluted motor populations, respectively. (C and D) Retrograde, stop, and anterograde sub-population factor difference from base case (protein aggregation with no defects) for 10%, 30%, 50%, 70%, and 90%, depletion and dilution severities, respectively.

retrograde sub-populations did not substantially change between the 70% and 90% severity depleted cases.

The cargo state analysis for either the depleted kinesin *or* dynein populations is shown in Fig. 9A and C. The cargo state analysis for depleted kinesin (Fig. 9A) is not intuitive. Depleting kinesin results in a decrease in retrogradely transported cargos at impairment severities less than or equal to 50%, and a sharp increase in retrograde cargos at only the most severe impairment severities (e.g. 90%). Stopped cargos increase as a function of impairment severity. Anterograde cargos initially remain practically unchanged at kinesin depletion severities $<50\%$, and sharply decrease at severities $>50\%$. Depleting dynein (Fig. 9C) results in an approximate 10–16% increase in anterograde cargos at dynein depletion severities $<50\%$ and a sharp increase in anterograde cargos only at the most severe dynein depletion (90%). Stopped cargos initially increase ($+21\%$ compared to base case at 10% dynein depletion), decrease slightly at mid-severities (-6% at 50% dynein depletion), and decrease sharply at the most severe dynein depletion (-86% at 90% dynein depletion compared to base case).

The cargo state analysis for the simultaneously diluted kinesin *and* dynein motor population(s) is shown in Fig. 8B and D. For the 10% severity diluted case, there is approximately a 7% decrease in the retrograde sub-population and an approximate 10% increase in the stop sub-population; the anterograde sub-population remained essentially the same as the base case. For the 30% severity diluted case, there is an approximate 15% increase of the retrograde population from the base case and a nearly proportional decrease in the anterograde sub-population; however, the stop sub-population remained similar to the 10% severity case. At 50% severity, both the anterograde and retrograde sub-populations decreased by 22% and 29%, respectively, compared to base; correspondingly, the stop sub-population dramatically increased by 80% compared to base. For the 70% and 90% severity diluted cases, we saw further substantial decreases in the anterograde and retrograde populations and proportional decreases in the stop sub-populations. Thus, while the magnitudes for the anterograde to retrograde sub-populations dramatically drop from 70% to 90% severity, their ratio did not substantially change between these two diluted cases.

Diluting only kinesin (Fig. 9B) *or* dynein (Fig. 9D), results in very different respective trends identified in cargo state analysis. Kinesin dilution results in a slight increase of retrograde transport at low impairment severities (e.g. $+15\%$ compared to base case at 10% dilution), tapers retrograde transport to near wild type levels at mid-level severities (-1% compared to base at 50% dilution), and increases retrograde transport at the most impaired severities ($+73\%$ compared to base at 90% dilution). With kinesin dilution, stopped cargos decrease at low severities (e.g. -13% at 10% dilution compared to wild type) and increase compared to wild type at greater severities. Dynein dilution results in a steady increase in anterograde transport with dilution severity, and a corresponding steady decrease in stopped cargos.

3.2.3. *Correlation matrices (e.g. "landscapes") provide a mechanistic fingerprint*

Many measures have been utilized to examine and quantify physiological axonal transport. Such measures are often seen less in pathological experimental examination of axonal transport, likely because axonal transport is just one of several topics being examined in typical experimental models, such as the SOD1 mouse model of ALS. However, having a barrage of metrics is still nonetheless invaluable. Fig. 10A and B, illustrates the cross-correlation matrices or landscapes for the depleted and diluted cases. We performed a sensitivity analysis, running each simulation for 4.7 s (the time window utilized by experimental studies) to quantify the changes in outcome measures. Theses outcome metrics, along with a few pertinent input parameters, were then cross-correlated with one another to obtain the landscapes shown (see Section 2 and our previous work (Mitchell and Lee, 2007, 2008)). Table 2 defines the measures utilized in the landscapes.

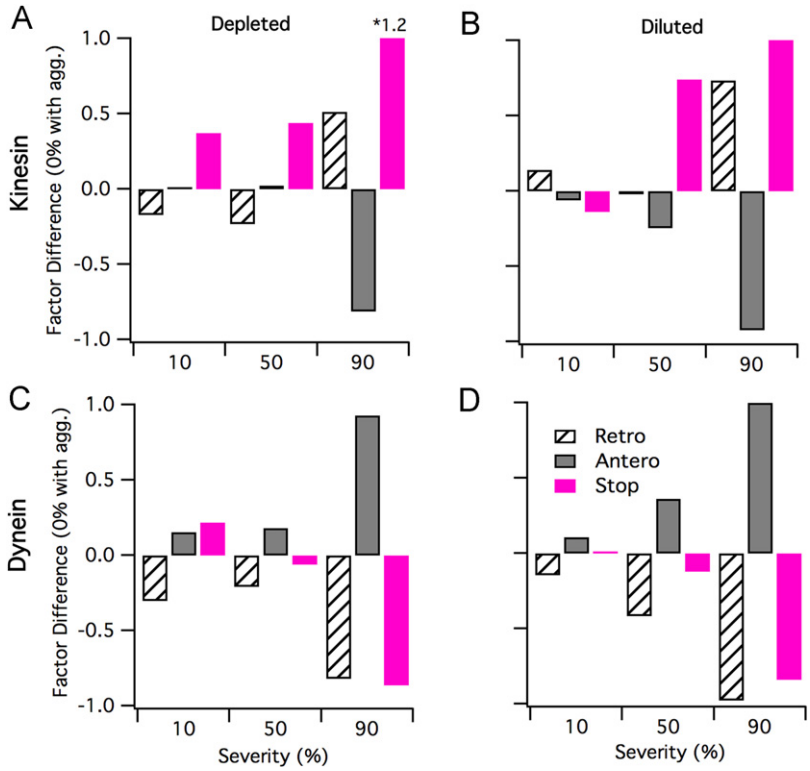

Fig. 9. Cargo state analysis for depletion and dilution impairments that affect *either* kinesin or dynein. (A and C) Retrograde, stop, and anterograde sub-population factor difference from base case (protein aggregation with no defects) for 10%, 50%, and 90% depletion severities. (B and D) Retrograde, stop, and anterograde sub-population factor difference from base case (protein aggregation with no defects) for 10%, 50%, and 90% dilution severities.

By visual inspection, there are many similarities between the depleted and diluted cases. One major similarity is that correlations specific to kinesin, or anterograde transport, positively correlate with the experimental moving cargo velocity bins utilized by Brown and colleagues (Brown et al., 2005) to examine the slow transport of neurofilaments (see large section of red blocks in upper left-hand corner of Fig. 10A and B). Other major similarities include the correlations involving ATP, cargo size, and the stop sub-population (e.g. Brown0); these strongly and positively correlate with each other, loosely and positively correlate with average dynein/retrograde velocities, and negatively correlate with all kinesin/anterograde measures and all Brown velocity bin measures that are greater than zero.

The major differences between the depleted and diluted cases largely involve dynein/retrograde-related correlations. For example, there are many correlation sign flips, which involve DAvgVel (average velocity of retrogradely moving cargos) between the diluted and depleted cases; furthermore, there is a block of absent correlations in the diluted case where substantial negative correlations exist in the depleted case between DAvgVel and number of bound kinesin (KAvgNb), maximum position (MaxPos), and the larger Brown velocity bins. However, perhaps the most telling differences between the depleted and diluted landscapes are the correlations involving severity of defect. For the depleted case, severity substantially and positively correlates with the anterograde to retrograde sub-population ratio (KDratio) and the number of total pauses, while the KDRatio negatively correlates with pause duration (AvgPause). Note that the aforementioned correlations are the exact opposite for the diluted case.

Taken together, the above differences in correlations potentially indicate that it is the competition between kinesin and dynein that results in the differing effects or outcomes of the depleted and diluted cases. In particular, competition plays a greater role at the lower severities, which is why differences between the depleted and diluted cases are initially magnified. To an extent, less competition favors dynein, likely due to the fact that its stall force is much lower than that of kinesin. Thus, in general, the retrogradely transported cargos are more sensitive to defects. However, it would appear that the central impact of impairment, regardless of defect, is the disruption of the normal transport balance, that is, the ratio of anterograde to retrograde moving cargos. With increasing severity, as the number of functional motors is further depleted or diluted, competition becomes less of a factor; the system dynamics likely switch from being competition-driven to kinetics-driven. Hence, at the higher severities, relative further changes in the anterograde to retrograde sub-population ratios are not as evident. Rather, pausing and off-track state kinetics dominate, leading to soaring stop-subpopulations and a corresponding plummet in retrograde and anterograde sub-populations.

4. Discussion

The inability to identify, discern, or distinguish among different possible axonal transport types has been a major obstacle in pathological axonal transport research. Scientists have had to rely on the introduction of engineered mutants or knockouts and compare their imposed transport impairments to those seen in actual experimental clinical pathologies, such as ALS, Alzheimer's or Huntington's, in hopes of finding a "match". However, in this study, we were able to quantitatively discern three different general axonal transport impairments from one another (cargo protein aggregation, motor depletion, and motor dilution) utilizing typical experimental measures of axonal transport. Our results reveal that these general impairment types can be distinguished using a combination of cargo distributions, cargo state analysis, and cross-correlation landscapes of experimental measures.

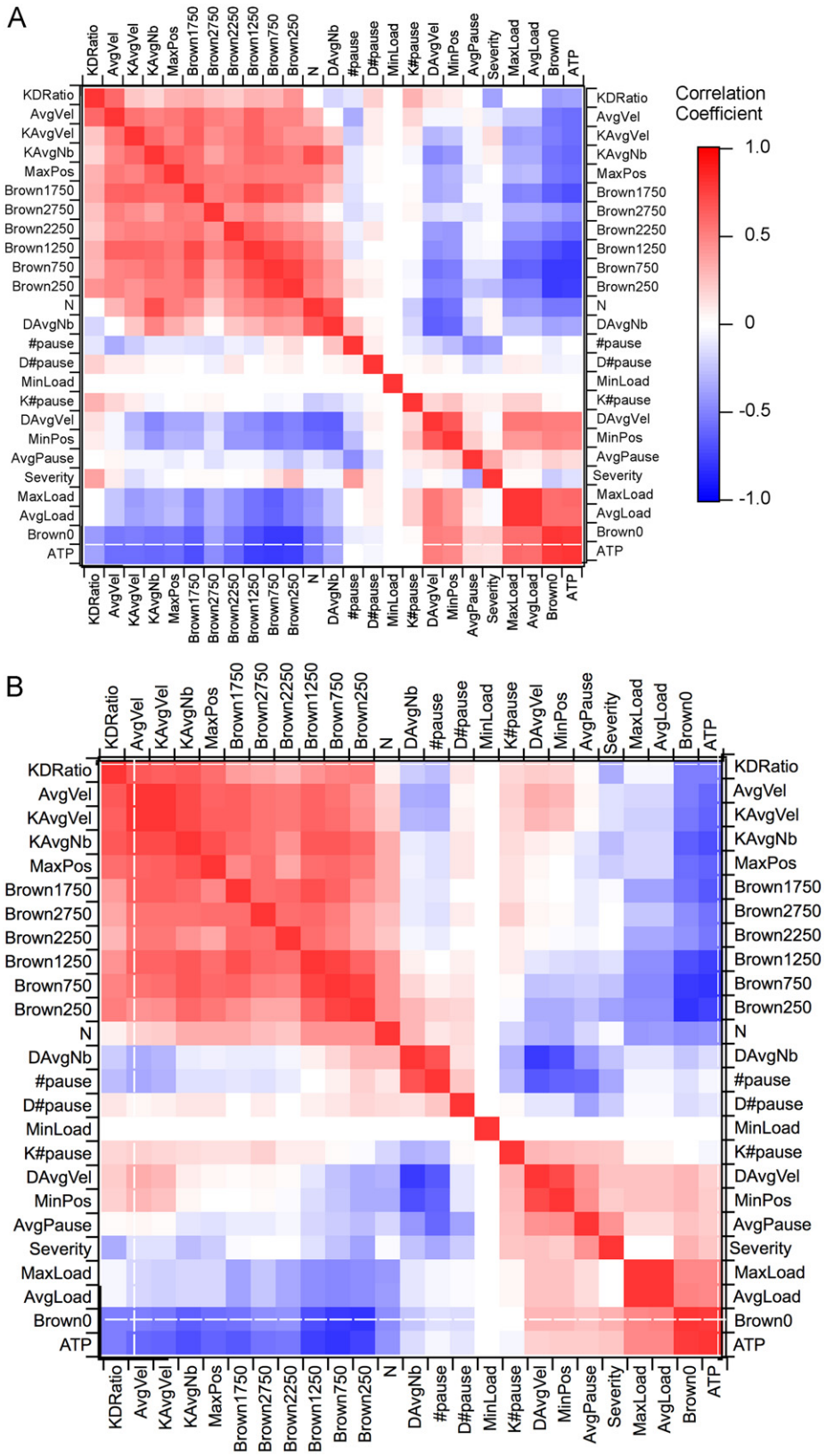

Fig. 10. Landscape comparison of quantitative measures for depleted and diluted motor populations. The landscapes represent the cross-correlation values of a few key input parameters as well as quantified outcome measures for each simulation. Measures, which were derived from the experimental physiological axonal transport literature, are described in Table 1. (A) Depleted motor population landscape. (B) Diluted motor population landscape.

By conceptually implementing specific axonal transport defects within a mechanistic computational axonal transport model, we have identified the potential "experimental fingerprints" of protein aggregation, simultaneous kinesin and dynein motor population depletion, and simultaneous kinesin and dynein motor population dilution. With protein aggregation alone, cargo distributions become

more unimodal, and cargo state analysis reveals a decrease in retrograde cargos, no change in anterograde cargo, and an increase in the stop sub-population. In the case of a depleted motor population, the number of total cargos moving decreases, but the positional range and velocities of the cargo distribution remains the same. In the case of a diluted motor population, the cargo distribution reveals fewer moving cargos as well as decrease in their positional range and velocity. Finally, cargo state analysis and cross-correlation landscapes, together, reveal that the different initial directional cargo fluctuations with increasing severity between depleted and diluted motor populations result from changes in competition between kinesin and dynein, which ultimately change the ratio of anterogradely to retrogradely moving cargos.

4.1. Evidence for SOD1 axonal transport defect type

Experimental evidence reveals several clues regarding the possible SOD1 impairment type: experimental data reveals that retrograde transport deficits appear first, at the asymptomatic stage (Bilsland et al., 2010; Shi et al., 2010). Simultaneously, experimental evidence has revealed a decreased presence of kinesin in young transgenic mice while older transgenic mouse have decreased kinesin and dynein (Zhang et al., 1997; Warita et al., 1999). In conjunction, genetic analysis also reveals a decrease in expression of kinesin-related mRNA (Pantelidou et al., 2007). Additionally, a study examining transport of individually labeled mitochondria found that there is an overall increase in pausing of anterograde and retrograde cargos at all time points (Sasaki et al., 2005). Another study examining mitochondria transport found decreases in both anterograde and retrograde transport in membrane-bound organelles, but only a reduction of anterograde transport of mitochondria (De Vos et al., 2007). Also, a study examining axonal transport of acetylcholine found that over-expressing kinesin in the SOD1 model prevented axonal transport deficits (Teuchert et al., 2006; Tateno et al., 2009). Finally, two studies that crossed two different dynein mutants (Loa and Cra1) with a mutant SOD1 mouse model showed a complete reversal of axonal transport deficits (Kieran et al., 2005). Individually, Loa and Cra1, cause retrograde transport deficits due to the mutations' negative impact on dynein; however, crossing either a Loa (Kieran et al., 2005) or Cra1 (Teuchert et al., 2006) mouse with an SOD1 transgenic mouse prevents both the typical anterograde and retrograde transport deficits that are typically seen in the SOD1 transgenic ALS mouse model. Until now, the results of the mutant cross-breeding studies have befuddled the field. However, the model presented here gives insight, collectively, into the aforementioned results (see below).

Based on the results presented here, protein aggregation with depletion is the scenario that best aligns with the above experimental evidence. Protein aggregation alone or protein aggregation concomitant with kinesin depletion are the only cases that initially (e.g. at lower impairment severities, corresponding to the asymptomatic time points) result in retrograde-specific deficits in combination with increased cargo pausing (stopped cargos). At later time points (e.g. higher impairment severities), the SOD1 transport defect type most aligns with an impairment affecting both the kinesin and dynein populations, namely depletion. The presented model data predict depletion of both motor populations at higher severities given that cargo state analysis revealed decreased anterograde and retrograde transport with increased pausing/stopped cargos at $>50\%$ depletion.

With its higher stall force, the kinesin population is typically smaller than the dynein population, making it initially more vulnerable to depletion. In fact, protein aggregation, itself, could initially lead to kinesin depletion by increasing the number of motors required to move the enlarged cargos. Depletion of dynein at later time points (e.g. higher impairment severities) is likely due to the decreased transport of dynein by the depleted kinesin population, which would ultimately deplete both motor populations, as has been seen experimentally in older SOD1 mice (Warita et al., 1999). Finally, kinesin depletion would best explain the results that increased kinesin expression or crossbreeding with dynein mutants (that lower the effective dynein population) result in restoring the balance between anterograde and retrograde transport. In fact, oscillations in physiological processes, including axonal transport, have been previously noted in the G93A mouse model of ALS (Mitchell and Lee, 2012).

4.2. No correlation between transport speed or cargo type

There have been different hypotheses regarding which transport types (e.g. fast versus slow transport) and which cargo types and/or sizes are more prone to axonal transport defects (Zhang et al., 1997; Sasaki et al., 2004; De Vos et al., 2008). Experimentally, while some cargo types appear to be more affected, no direct correlation has been found showing impairments are specific to a certain cargo type (Williamson and Cleveland, 1999). In this study, we examined a broad range of transport, slow through bi-directional, over a large range of cargo sizes. We did not find any direct, quantitative correlation with transport type or load size with protein aggregation or the severity of depletion or dilution. However, qualitatively, changes in position of smaller cargos with impairment were visually easier to notice since smaller cargos typically go further distances, as has been seen experimentally. Based on the results of this study, if there are specific fast transport, slow transport, or cargo-specific impairment defects, they are not inherent or emergent from the motor dynamics, themselves. Rather, they would likely be due to defects of the cargo adapter proteins, such the mitochondrial adapter Milton, or specific chemical mediators, such as tau or phosphorylation.

4.3. Impact of kinesin and dynein interdependence

Physiological studies have cited the impact of kinesin and dynein interdependence (Martin et al., 1999; Kural et al., 2005). Mutating or impairing one motor type results in changes in both anterograde and retrograde transport. Indeed, the landscapes of cross-correlations presented in the results of this study indicate that the ratio of anterograde to retrograde transport seems to be a key determinant of pathological impairment, whether the motor population was depleted or diluted. Thus, one hypothesis is that the key underlying mechanism of pathological axonal transport is disruption of this balance. Hence, treating kinesin depletion in the SOD1 mouse with a dynein mutant resulted in an effective treatment in the experimental SOD1/Loa and SOD1/Cra mouse. Thus, the balance between anterograde and retrograde transport may be more important the magnitude of transport for either direction. Moving forward, a better understanding of kinesin and dynein cooperative transport and population regulation could be critical to solving the mysteries of pathological transport.

4.4. Model limitations

Specific cooperativity schemes other than the one utilized here (see Methods) could give additional insight into the results presented here, namely the implication of the presented results on the interaction between kinesin and dynein. Additionally, as a disease progresses, the injured neuron could utilize anterograde or retrograde transport to alter signaling and transport feedback (Kam et al., 2009), an aspect not included in this model. Also, an increase in cargo size, such as is seen with protein aggregation,

could potentially change cargo-anchoring dynamics, which have an impact on motor-cargo binding and unbinding rates (Erickson et al., 2011) not considered in this work. Finally, motor type regulators, like dynactin, tau, Lis1, JIP3 were not specifically included. However, the overall effects of such regulators, which impose changes in velocity, directionality, processivity, and load size specificity to cargos, were individually and collectively examined in the sensitivity analysis. Neither the aforementioned overall regulator effects nor their affected kinetic parameter changes substantially altered the findings of this study (not shown). Finally, including a feedback loop to examine transport of the motors themselves, could give insight into how kinesin depletion could lead to dynein depletion.

Acknowledgments

This work was supported by the National Institute of Health (NS069616 and NS062200).

References

Ackerley, S., et al., 2000. Glutamate slows axonal transport of neurofilaments in transfected neurons. J. Cell Biol. 150 (1), 165–176.
Ackerley, S., et al., 2003. Neurofilament heavy chain side arm phosphorylation regulates axonal transport of neurofilaments. J. Cell Biol. 161 (3), 489–495.
Baloh, R.H., et al., 2007. Altered axonal mitochondrial transport in the pathogenesis of Charcot-Marie-Tooth disease from mitofusin 2 mutations. J. Neurosci. 27 (2), 422–430.
Banks, J., et al., 2005. Discrete-Event System Simulation USA. Pearson Education.
Barkus, R.V., et al., 2008. Identification of an axonal kinesin-3 motor for fast anterograde vesicle transport that facilitates retrograde transport of neuropeptides. Mol. Biol. Cell 19 (1), 274–283.
Bilsland, L.G., et al., 2010. Deficits in axonal transport precede ALS symptoms in vivo. Proc. Natl. Acad. Sci. U S A 107 (47), 20523–20528.
Brady, S.T., 1985. A novel brain ATPase with properties expected for the fast axonal transport motor. Nature 317 (6032), 73–75.
Brown, A., et al., 2005. Stochastic simulation of neurofilament transport in axons: the "stop-and-go" hypothesis. Mol. Biol. Cell 16 (9), 4243–4255.
Brownlees, J., et al., 2002. Charcot-Marie-Tooth disease neurofilament mutations disrupt neurofilament assembly and axonal transport. Hum. Mol. Genet. 11 (23), 2837–2844.
Cai, Q., et al., 2011. Regulation of axonal mitochondrial transport and its impact on synaptic transmission. Neurosci. Res. 70 (1), 9–15.
Craciun, G., et al., 2005. A dynamical system model of neurofilament transport in axons. J. Theor. Biol. 237 (3), 316–322.
De Vos, K.J., et al., 2007. Familial amyotrophic lateral sclerosis-linked SOD1 mutants perturb fast axonal transport to reduce axonal mitochondria content. Hum. Mol. Genet. 16 (22), 2720–2728.
De Vos, K.J., et al., 2008. Role of axonal transport in neurodegenerative diseases. Annu. Rev. Neurosci. 31, 151–173.
Elam, J.S., et al., 2003. Amyloid-like filaments and water-filled nanotubes formed by SOD1 mutant proteins linked to familial ALS. Nat. Struct. Biol. 10 (6), 461–467.
Ellis, D.Z., et al., 2003. Global loss of Na,K-ATPase and its nitric oxide-mediated regulation in a transgenic mouse model of amyotrophic lateral sclerosis. J. Neurosci. 23 (1), 43–51.
Erickson, R.P., et al., 2011. How molecular motors are arranged on a cargo is important for vesicular transport. PLoS Comput. Biol. 7 (5), e1002032.
Feany, M.B., La Spada, A.R., 2003. Polyglutamines stop traffic: axonal transport as a common target in neurodegenerative diseases. Neuron 40 (1), 1–2.
Fergani, A., et al., 2011. A mutation in the dynein heavy chain gene compensates for energy deficit of mutant SOD1 mice and increases potentially neuroprotective IGF-1. Mol. Neurodegener. 6 (1), 26.
Ferreirinha, F., et al., 2004. Axonal degeneration in paraplegin-deficient mice is associated with abnormal mitochondria and impairment of axonal transport. J. Clin. Invest. 113 (2), 231–242.
Gao, Y.Q., 2006. A simple theoretical model explains dynein's response to load. Biophys. J. 90 (3), 811–821.
Gazzola, M., et al., 2009. A stochastic model for microtubule motors describes the in vivo cytoplasmic transport of human adenovirus. PLoS Comput. Biol. 5 (12), e1000623.
Gunawardena, S., Goldstein, L.S., 2001. Disruption of axonal transport and neuronal viability by amyloid precursor protein mutations in Drosophila. Neuron 32 (3), 389–401.
Hart, P.J., 2006. Pathogenic superoxide dismutase structure, folding, aggregation and turnover. Curr. Opin. Chem. Biol. 10 (2), 131–138.
Ittner, L.M., et al., 2008. Parkinsonism and impaired axonal transport in a mouse model of frontotemporal dementia. Proc. Natl. Acad. Sci U S A 105 (41), 15997–16002.
Jiang, Y.M., et al., 2005. Gene expression profile of spinal motor neurons in sporadic amyotrophic lateral sclerosis. Ann. Neurol. 57 (2), 236–251.
Julien, J.P., Mushynski, W.E., 1998. Neurofilaments in health and disease. Prog. Nucleic Acid Res. Mol. Biol. 61, 1–23.
Kam, N., et al., 2009. Can molecular motors drive distance measurements in injured neurons? PLoS Comput. Biol. 5 (8), e1000477.
Kasher, P.R., et al., 2009. Direct evidence for axonal transport defects in a novel mouse model of mutant spastin-induced hereditary spastic paraplegia (HSP) and human HSP patients. J. Neurochem. 110 (1), 34–44.
Kieran, D., et al., 2005. A mutation in dynein rescues axonal transport defects and extends the life span of ALS mice. J. Cell Biol. 169 (4), 561–567.
Kim, J., et al., 2011. Quantitative in vivo measurement of early axonal transport deficits in a triple transgenic mouse model of Alzheimer's disease using manganese-enhanced MRI. Neuroimage 56 (3), 1286–1292.
Klumpp, S., Lipowsky, R., 2005. Cooperative cargo transport by several molecular motors. Proc. Natl. Acad. Sci. U S A 102 (48), 17284–17289.
Kural, C., et al., 2005. Kinesin and dynein move a peroxisome in vivo: a tug-of-war or coordinated movement? Science 308 (5727), 1469–1472.
Kuznetsov, A.V., 2010. Effect of vesicle traps on traffic jam formation in fast axonal transport. Math. Biosci. 226 (2), 147–155.
LaMonte, B.H., et al., 2002. Disruption of dynein/dynactin inhibits axonal transport in motor neurons causing late-onset progressive degeneration. Neuron 34 (5), 715–727.
LaPointe, N.E., et al., 2009. The amino terminus of tau inhibits kinesin-dependent axonal transport: implications for filament toxicity. J. Neurosci. Res. 87 (2), 440–451.
Lee, W.C., et al., 2004. Cytoplasmic aggregates trap polyglutamine-containing proteins and block axonal transport in a Drosophila model of Huntington's disease. Proc. Natl. Acad. Sci. U S A 101 (9), 3224–3229.
Magrane, J., Manfredi, G., 2009. Mitochondrial function, morphology, and axonal transport in amyotrophic lateral sclerosis. Antioxid. Redox Signal. 11 (7), 1615–1626.
Martin, M., et al., 1999. Cytoplasmic dynein, the dynactin complex, and kinesin are interdependent and essential for fast axonal transport. Mol. Biol. Cell 10 (11), 3717–3728.
Miller, C.C., et al., 2002. Axonal transport of neurofilaments in normal and disease states. Cell Mol. Life Sci. 59 (2), 323–330.
Misko, A., et al., 2010. Mitofusin 2 is necessary for transport of axonal mitochondria and interacts with the Miro/Milton complex. J. Neurosci. 30 (12), 4232–4240.
Mitchell, C.S., et al., 2007. An analysis of glutamate spillover on the N-methyl-D-aspartate receptors at the cerebellar glomerulus. J. Neural Eng. 4 (3), 276–282.
Mitchell, C.S., Lee, R.H., 2007. Output-based comparison of alternative kinetic schemes for the NMDA receptor within a glutamate spillover model. J. Neural Eng. 4 (4), 380–389.
Mitchell, C.S., Lee, R.H., 2008. Pathology dynamics predict spinal cord injury therapeutic success. J. Neurotrauma 25 (12), 1483–1497.
Mitchell, C.S., Lee, R.H., 2009. A quantitative examination of the role of cargo-exerted forces in axonal transport. J. Theor. Biol. 257 (3), 430–437.
Mitchell, C.S., Lee, R.H., 2012. Dynamic meta-analysis as a therapeutic prediction tool for amyotrophic lateral sclerosis. In: Maurer, M.H. (Ed.), Amyotrophic Lateral Sclerosis. InTech.
Morfini, G., et al., 2002. Fast axonal transport misregulation and Alzheimer's disease. Neuromolecular Med. 2 (2), 89–99.
Morfini, G.A., et al., 2009a. Axonal transport defects in neurodegenerative diseases. J. Neurosci. 29 (41), 12776–12786.
Morfini, G.A., et al., 2009b. Pathogenic huntingtin inhibits fast axonal transport by activating JNK3 and phosphorylating kinesin. Nat. Neurosci. 12 (7), 864–871.
Muller, M.J., et al., 2008. Tug-of-war as a cooperative mechanism for bidirectional cargo transport by molecular motors. Proc. Natl. Acad. Sci. U S A 105 (12), 4609–4614.
Pantelidou, M., et al., 2007. Differential expression of molecular motors in the motor cortex of sporadic ALS. Neurobiol. Dis. 26 (3), 577–589.
Saha, A.R., et al., 2004. Parkinson's disease alpha-synuclein mutations exhibit defective axonal transport in cultured neurons. J. Cell Sci. 117 (Pt 7), 1017–1024.
Sasaki, S., et al., 2004. Slow component of axonal transport is impaired in the proximal axon of transgenic mice with a G93A mutant SOD1 gene. Acta Neuropathol. 107 (5), 452–460.
Sasaki, S., et al., 2005. Impairment of axonal transport in the axon hillock and the initial segment of anterior horn neurons in transgenic mice with a G93A mutant SOD1 gene. Acta Neuropathol. 110 (1), 48–56.
Sau, D., et al., 2011. Dysregulation of axonal transport and motorneuron diseases. Biol. Cell 103 (2), 87–107.
Shapiro, N.P., Lee, R.H., 2007. Synaptic amplification versus bistability in motoneuron dendritic processing: a top-down modeling approach. J. Neurophysiol. 97 (6), 3948–3960.
Shi, P., et al., 2010. Effects of ALS-related SOD1 mutants on dynein- and KIF5-mediated retrograde and anterograde axonal transport. Biochim. Biophys. Acta 1802 (9), 707–716.
Sinadinos, C., et al., 2009. Live axonal transport disruption by mutant huntingtin fragments in Drosophila motor neuron axons. Neurobiol. Dis. 34 (2), 389–395.
Strom, A.L., et al., 2008. Retrograde axonal transport and motor neuron disease. J. Neurochem. 106 (2), 495–505.
Tateno, M., et al., 2009. Mutant SOD1 impairs axonal transport of choline acetyltransferase and acetylcholine release by sequestering KAP3. Hum. Mol. Genet. 18 (5), 942–955.

Teuchert, M., et al., 2006. A dynein mutation attenuates motor neuron degeneration in SOD1(G93A) mice. Exp. Neurol. 198 (1), 271–274.
Wang, L., Brown, A., 2001. Rapid intermittent movement of axonal neurofilaments observed by fluorescence photobleaching. Mol. Biol. Cell 12 (10), 3257–3267.
Wang, X., et al., 2010. Amyloid-beta-derived diffusible ligands cause impaired axonal transport of mitochondria in neurons. Neurodegener. Dis. 7 (1–3), 56–59.
Warita, H., et al., 1999. Selective impairment of fast anterograde axonal transport in the peripheral nerves of asymptomatic transgenic mice with a G93A mutant SOD1 gene. Brain Res. 819 (1–2), 120–131.
Williamson, T.L., Cleveland, D.W., 1999. Slowing of axonal transport is a very early event in the toxicity of ALS-linked SOD1 mutants to motor neurons. Nat. Neurosci. 2 (1), 50–56.
Xia, C.H., et al., 2003. Abnormal neurofilament transport caused by targeted disruption of neuronal kinesin heavy chain KIF5A. J. Cell Biol. 161 (1), 55–66.
Zhang, B., et al., 1997. Neurofilaments and orthograde transport are reduced in ventral root axons of transgenic mice that express human SOD1 with a G93A mutation. J. Cell Biol. 139 (5), 1307–1315.